JOUL, Volume *4*

Supplemental Information

Shallow Iodine Defects Accelerate the Degradation of α-Phase Formamidinium Perovskite

Shaun Tan, Ilhan Yavuz, Marc H. Weber, Tianyi Huang, Chung-Hao Chen, Rui Wang, Hao-Cheng Wang, Jeong Hoon Ko, Selbi Nuryyeva, Jingjing Xue, Yepin Zhao, Kung-Hwa Wei, Jin-Wook Lee, and Yang Yang

Supplemental Experimental Procedures

Surface treatment of perovskite

For surface treatment of perovskite, in accordance with a previous report,[1] solid I_2 was dissolved in isopropyl alcohol and stirred at 80°C for 7 days to form I_3^- in equilibrium with trace amounts of I^- and I_2 according to the equation:[1]

$$I_2 + I^- \leftrightarrow I_3^-$$

The solution was deposited onto the control perovskite at 5000 rpm for 30 s, followed by annealing at 100°C for 5 min. Due to the dynamic equilibrium where all three iodine related species are present, and to simplify the comparison, the solution concentrations are given in terms of equivalent concentration of atomic iodine, i.e. 10 mM of dissolved I_2 is labelled as '20 mM'.

First-principles surface energy calculations

The 2x2xL surfaces were formed along (001) by periodic slabs including 9 to 11 atomic layers for a surface separated by 20 Å of vacuum. To characterize the formation and stability of the $FAPbI_3$ surfaces we use surface energies described as follows: we first calculate the cleavage energy of the clean surface

$$\sigma^{clv} = \frac{1}{2}\left[E^{slab,unrel.}_{FA_m\,Pb_nI_l(FAPbI_3)_N} - \left(m\mu_{FA} + n\mu_{Pb} + l\mu_I + NE^{bulk}_{FAPbI_3}\right)\right]$$

where the first term is the energy of the unrelaxed slab, μ_{FA}, μ_{Pb} and μ_I are the chemical potentials and $E^{bulk}_{FAPbI_3} = \mu_{FA} + \mu_{Pb} + 3\mu_I$ is the energy of the bulk. The relaxation energy is then calculated from

$$\sigma^{rl} = (E^{slab,rel.}_{FA_m\,Pb_nI_l(FAPbI_3)_N} - E^{slab,unrel.}_{FA_m\,Pb_nI_l(FAPbI_3)_N})$$

where the first and second terms are the total energy of the relaxed and unrelaxed slabs, respectively. The surface energy is calculated by $\gamma = (\sigma^{clean} + \sigma^{rel})/A$, where A is the area of the surface. The results, presented in Figure S3, show that the FAI terminated surface is the most thermodynamically stable with the lowest surface energy ($\gamma^{surf} = 1.54\ eV/nm^2$).

Positron Annihilation Spectroscopy

Positrons are implanted into the sample at different incident kinetic energies (E_k). $E_k$is equivalent to a mean implantation depth *d* according to the empirical formula

$$d = \frac{0.04\ {E_k}^{1.6}}{\rho}\ (\frac{\mu m \cdot g}{cm^3 \cdot keV^{1.6}})$$

where ρ is the material density. A gamma ray spectrum of detected counts as a function of photon energy is collected at each energy. Positrons thermalize in the material within several picoseconds until annihilation from this free thermalization state or trap at neutral or negatively charged states and then annihilate from the trap into two near opposite direction gamma photons of Doppler shifted 0.511 MeV each after lifetimes on the order of 100 ps, which is much longer than the thermalization time. The annihilation photons carry the combined momentum (*p*) of the electron and the positron as Doppler shifts proportional to

$$\Delta E = \frac{1}{2}p_p c$$

where c is the speed of light, and p_p is the momentum in the direction of the photon (the perpendicular part results in tiny angular deviations from opposite). Thermalized positrons contribute very little to the total *p* value. Hence, the full-width-at-half-maximum (FWHM) of the annihilation spectrum becomes a measure of the electron *p* at the annihilation sites. A background rate is determined and subtracted from the photoelectric 511 keV peak to account for positronium generation. Following background

subtraction, the peak is then area normalized. The fraction of the signal in a narrow central region is the shape (S) parameter, which relates to low *p* delocalized electrons that increase in relative intensity at positron trap sites. The contribution from high *p* bound electrons which retain some of the atomic element character dominates in the wings of the annihilation line and is measured by the wing (W) parameter. Surface S (or W) parameters are extracted from right at the surface (E_k < 0.1 keV) minus epithermal estimate (also part of fitting). Bulk S (or W) parameters are obtained by fitting the asymptotic trend from 0.8 < E_k (keV) < 6 to a constant using the dedicated fitting software Vepfit.

Supplemental Figures

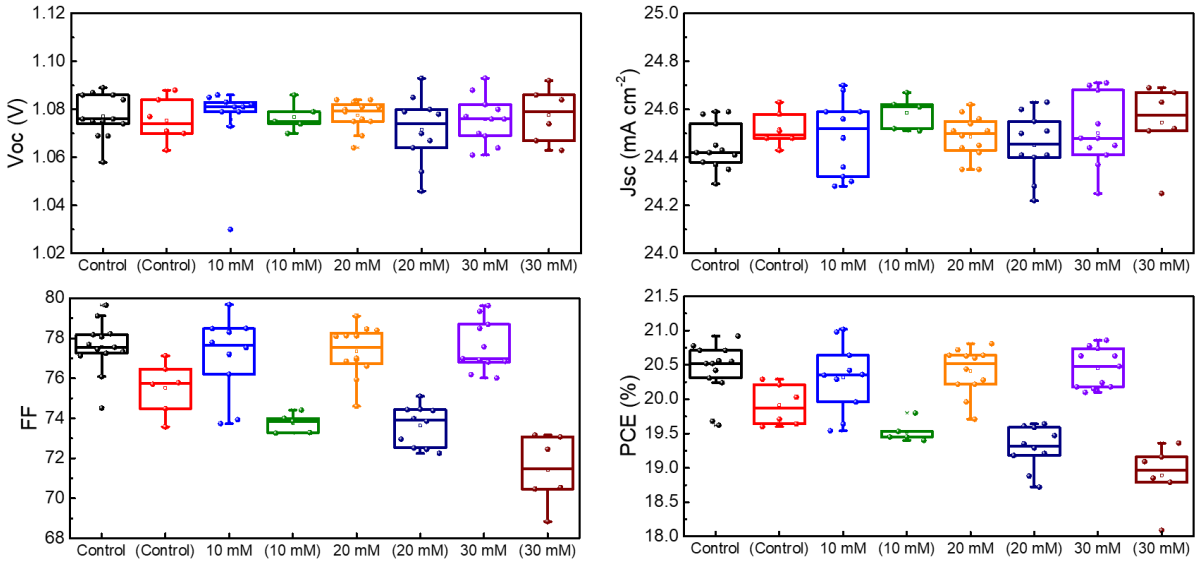

Figure S1 | Photovoltaic parameters of control and treated devices. Box plots showing the distribution of the open-circuit voltage (V_{OC}), short-circuit current density (J_{SC}), fill factor (FF), and power conversion efficiency (PCE) of the control and treated devices. Parenthesis indicate parameters measured in forward scan.

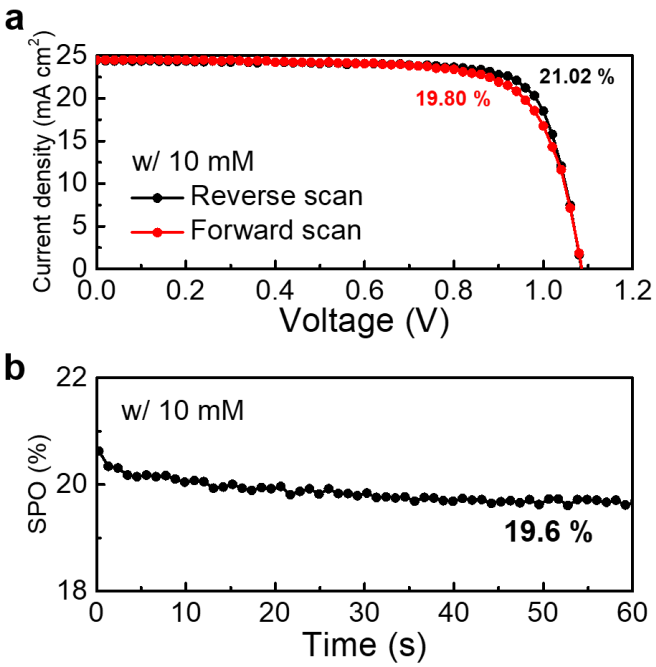

Figure S2 | Photovoltaic performance of treated devices. a, Current density and voltage (*J-V*) curves of the champion devices in reverse (1.2 V to -0.1 V) and forward (-0.1 V to 1.2 V) scan and **b,** stabilized power output (SPO).

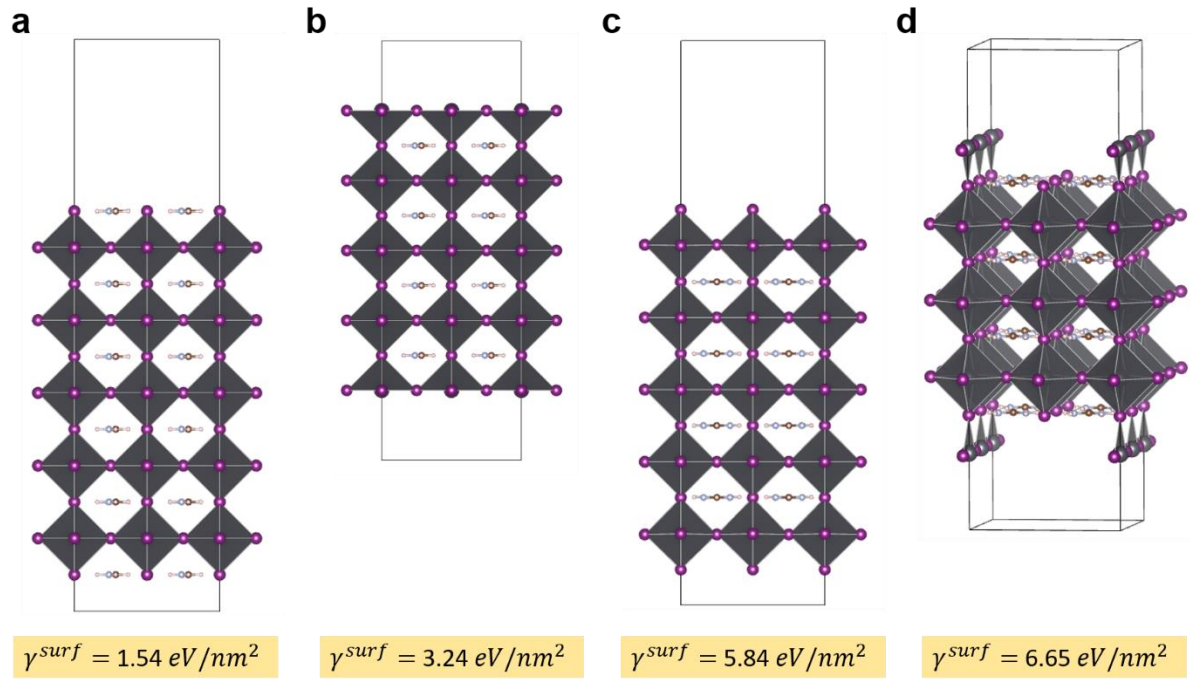

Figure S3 | Theoretical slab models for first-principles calculations. (001) slab models of $FAPbI_3$ perovskite with **a**, FAI, **b**, PbI_2 (flat), **c**, FAI with evaporated FA, and **d**, vacant termination. Their calculated respective surface energies (γ^{surf}) are included.

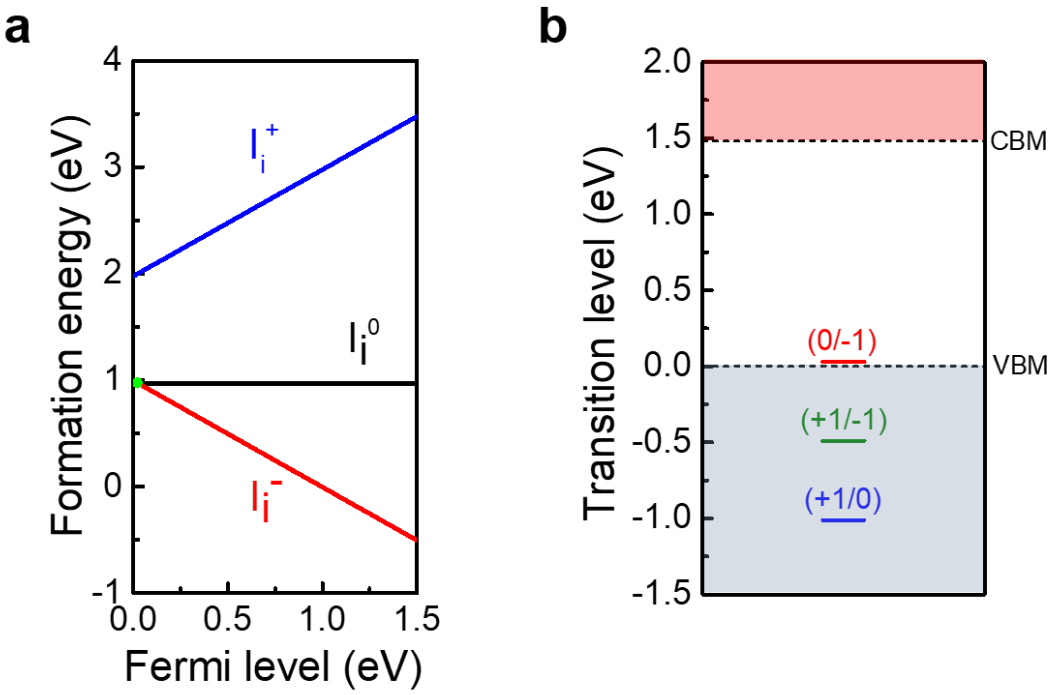

Figure S4 | Fermi level (E_F) dependence of the surface formation energies. a, E_F dependence of the surface formation energies of neutral and charged iodine interstitial point defects. Transition levels are marked with green dots. $E_F = 0$ is set at the valence band maximum. **b**, charge transition levels of I_i in $FAPbI_3$. Red and grey shaded areas mark the conduction band and valence band, respectively.

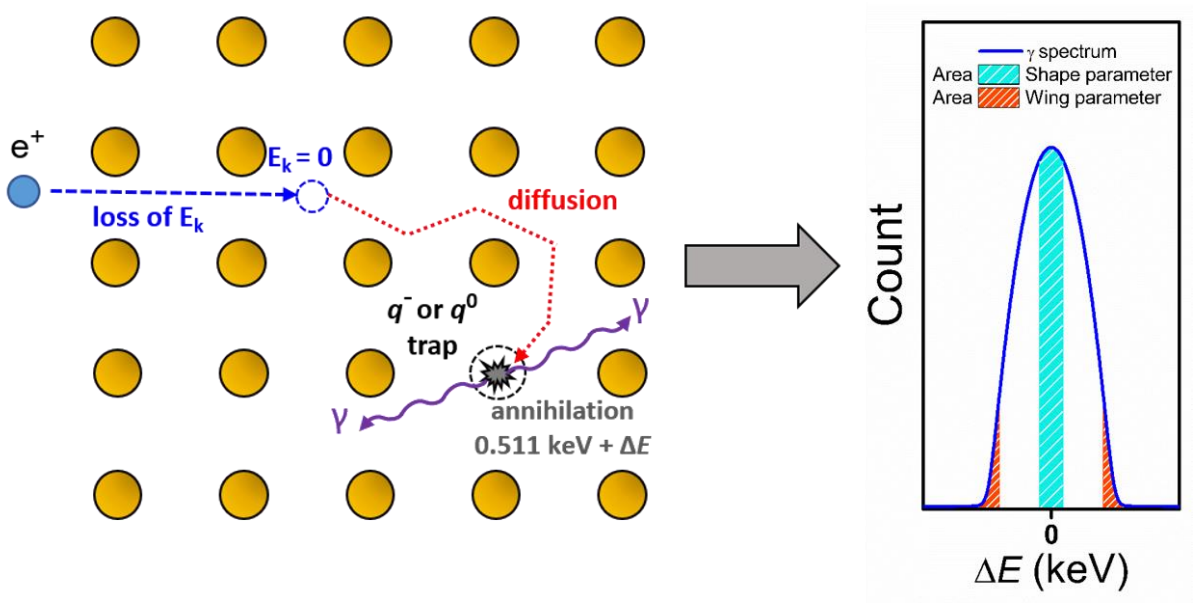

Figure S5 | Positron Annihilation Spectroscopy (PAS). Schematic of the PAS technique.

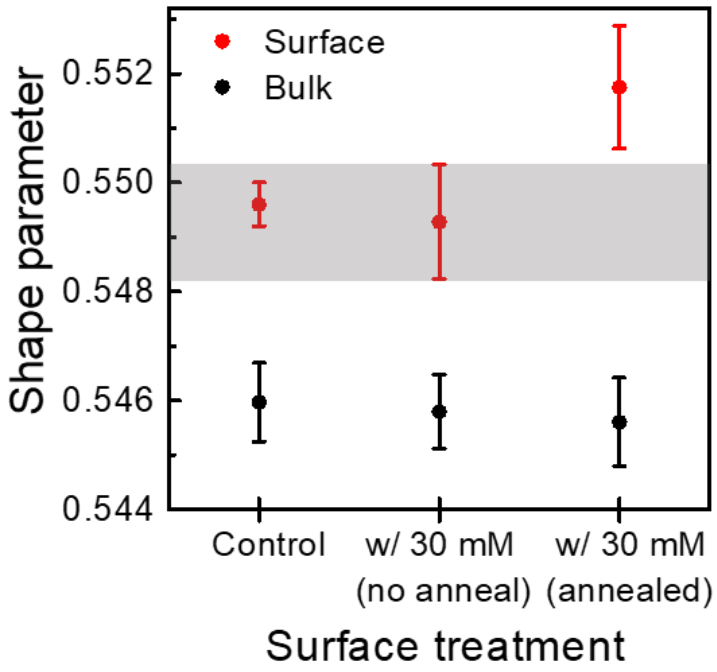

Figure S6 | Shape parameters of the perovskite films. Surface and bulk shape parameters of the control and treated perovskite films on glass. Grey highlighted area demarcates the upper and lower bounds of the 'w/ 30 mM (no anneal)' condition.

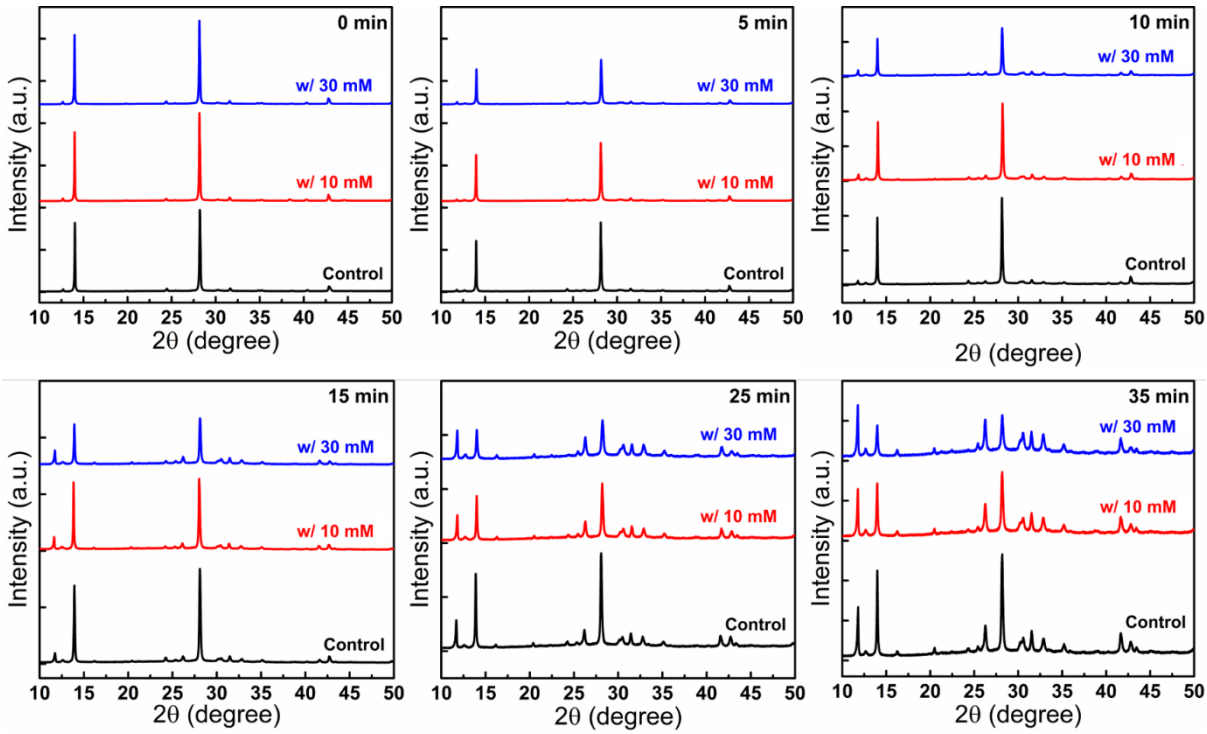

Figure S7 | X-ray diffraction (XRD) measurements on the perovskite films. XRD diffractograms of the control and treated perovskite films after different exposure times to iodine vapour.

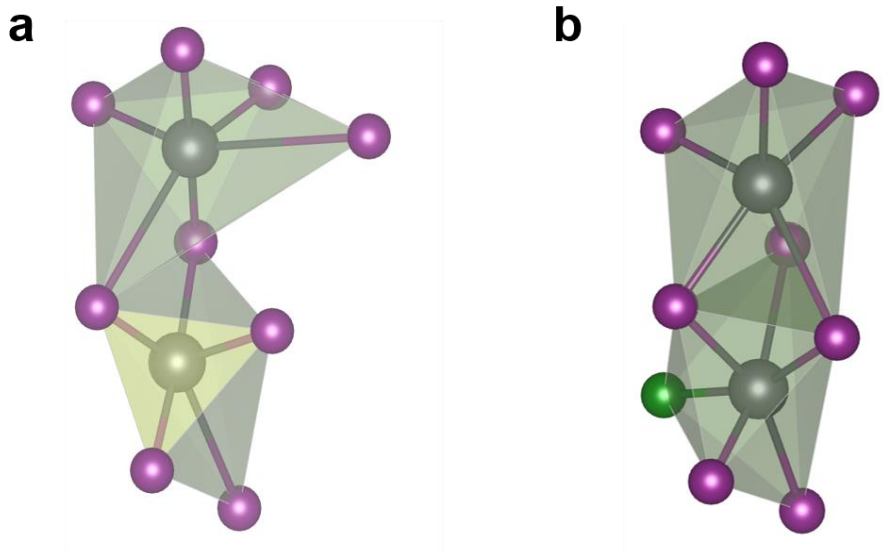

Figure S8 | Atomic coordination structures. Transition state atomic coordination for the **a**, defect-free, and **b**, with iodine interstitial (in green) lattices. Atoms are expressed by spheres; iodine (purple), and lead (grey).

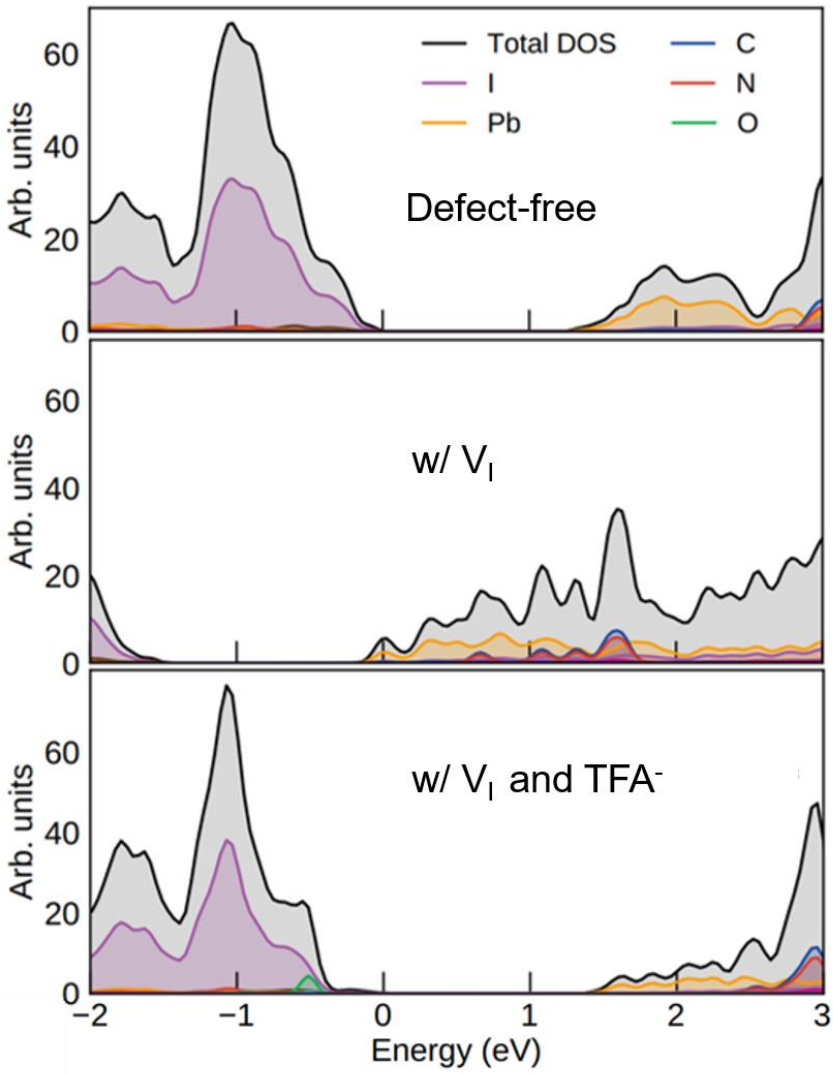

Figure S9 | Density of states (DOS) simulated with first-principles calculations. DOS of the defect-free, defected and passivated FAI-terminated surfaces.

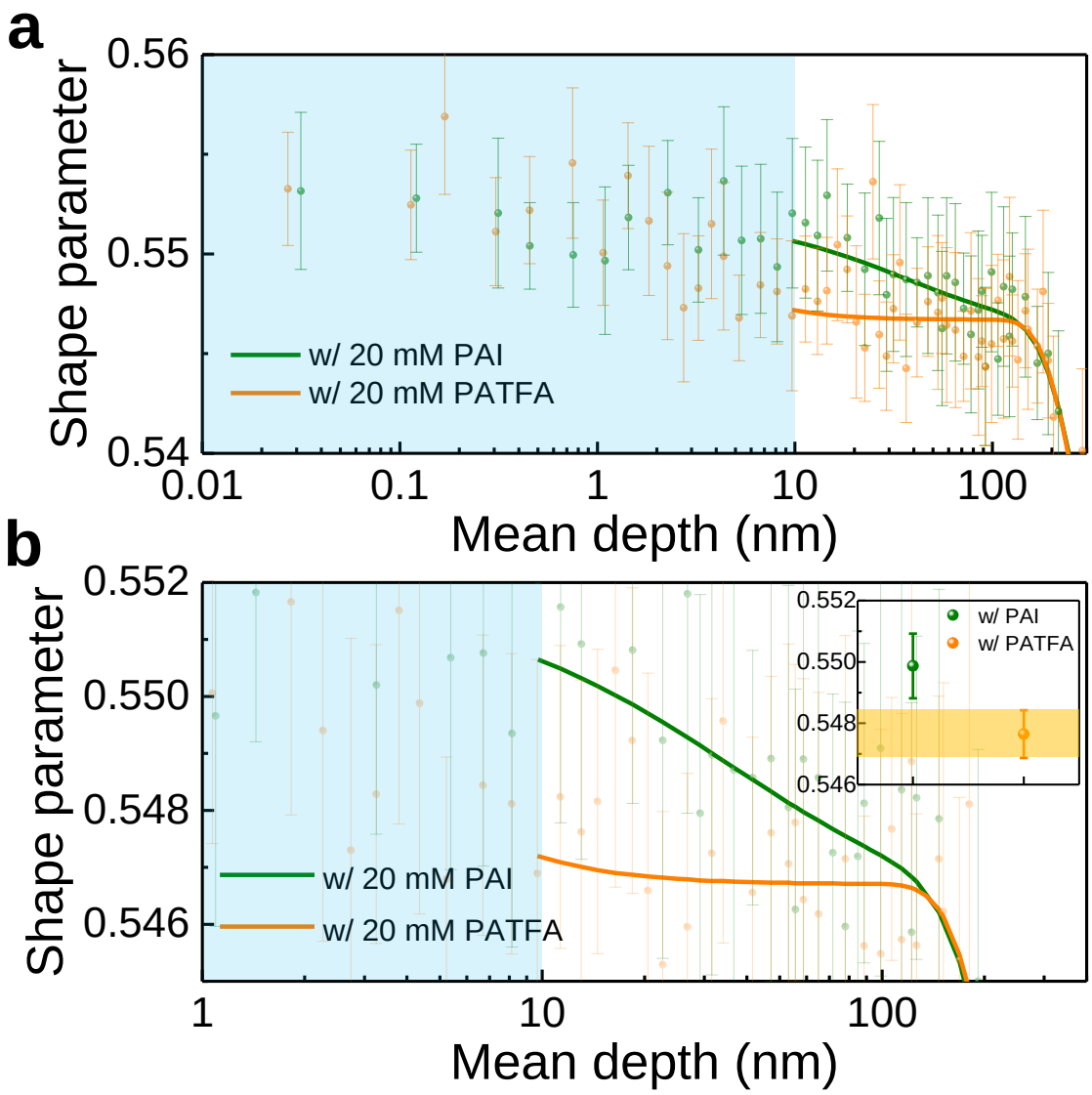

Figure S10 | Positron Annihilation Spectroscopy on treated perovskite films. a, Shape parameter as function of depth of perovskite films on glass treated with 20 mM of either PAI or PATFA. Blue shaded area indicates assumed passivation layer thickness based on previous report.[2] Lines are fitted using dedicated software Vepfit. **b**, Magnified region of (a). Inset shows the averaged shape parameter from the raw data points from mean depth of 10 to 50 nm in a running average series. Yellow shaded area demarcate the upper and lower bounds for the film treated with PATFA.

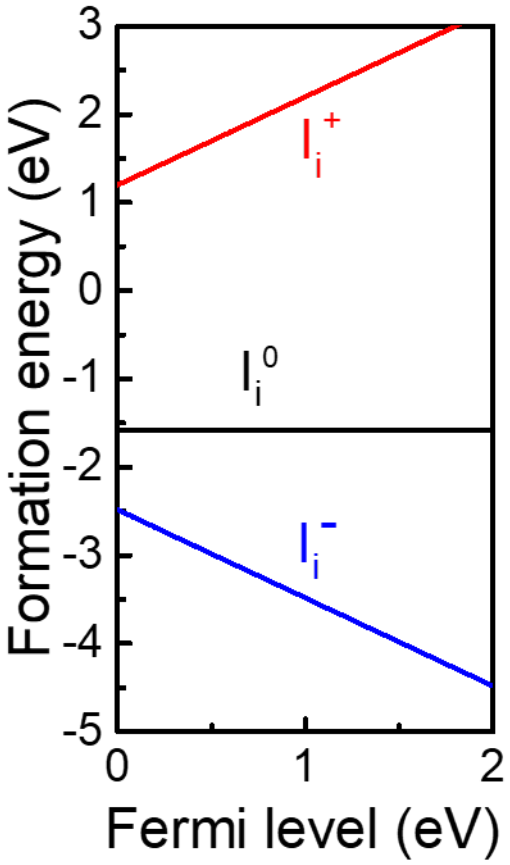

Figure S11 | Fermi level (E_F) dependence of the surface formation energies. a, E_F dependence of the surface formation energies of neutral and charged iodine interstitial point defects, calculated for a FAI-terminated $FAPbI_3$ slab with PA^+ cation as the capping layer. $E_F = 0$ is set at the valence band maximum.

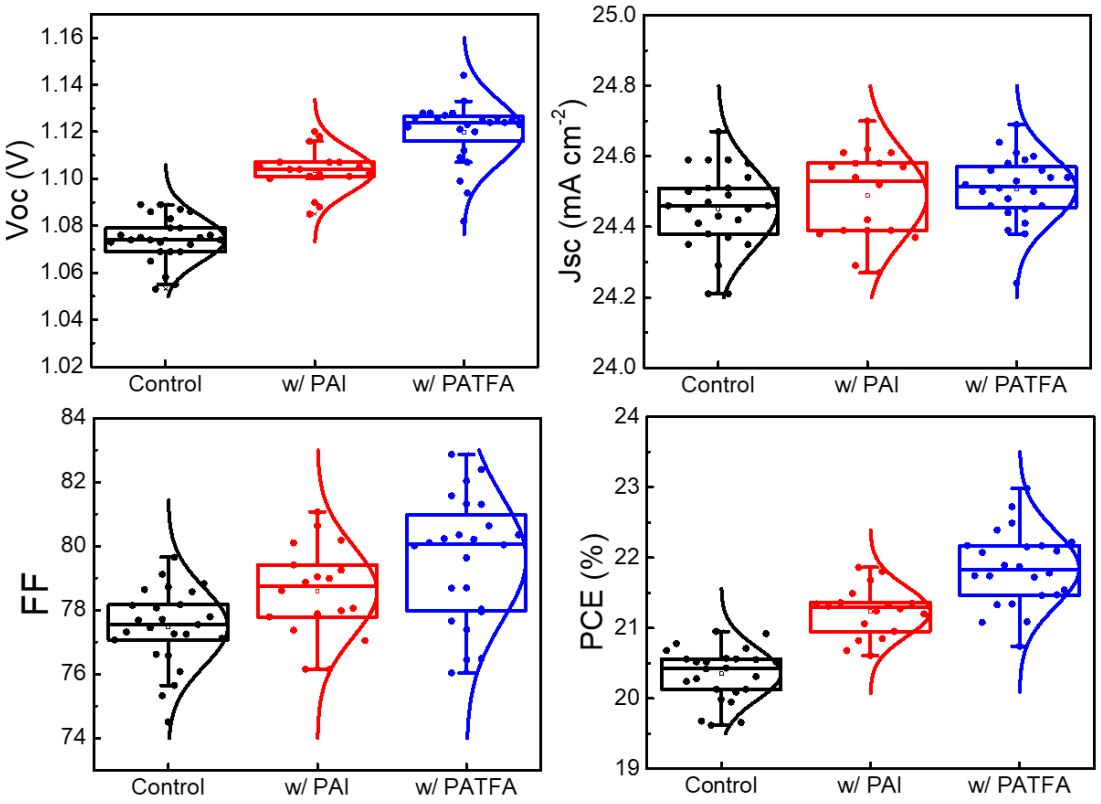

Figure S12 | Photovoltaic parameters of control and treated devices. Box plots showing the distribution of the open-circuit voltage (V_{OC}), short-circuit current density (J_{SC}), fill factor (FF), and power conversion efficiency (PCE) of the control and treated devices.

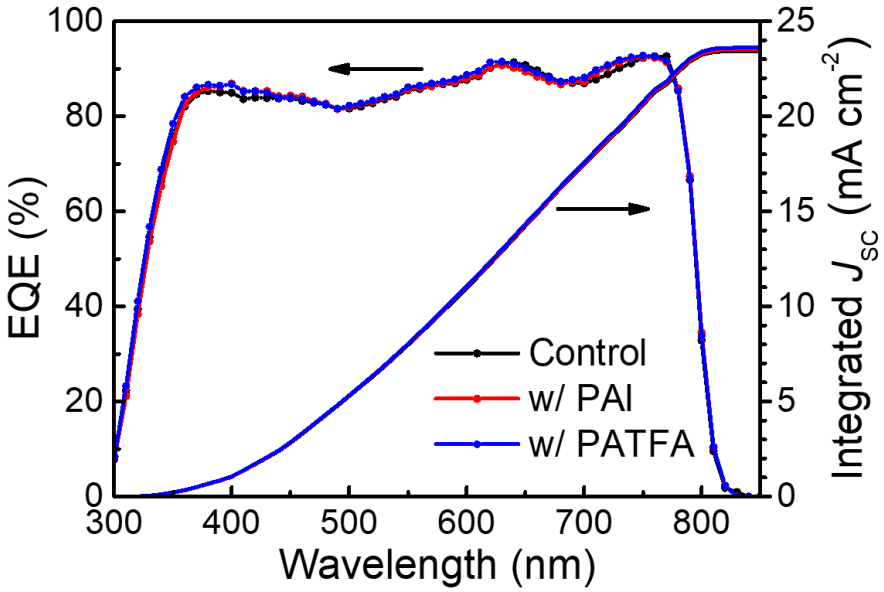

Figure S13 | Device external quantum efficiency (EQE) spectra. EQE spectra and integrated J_{SC} of the control and treated devices.

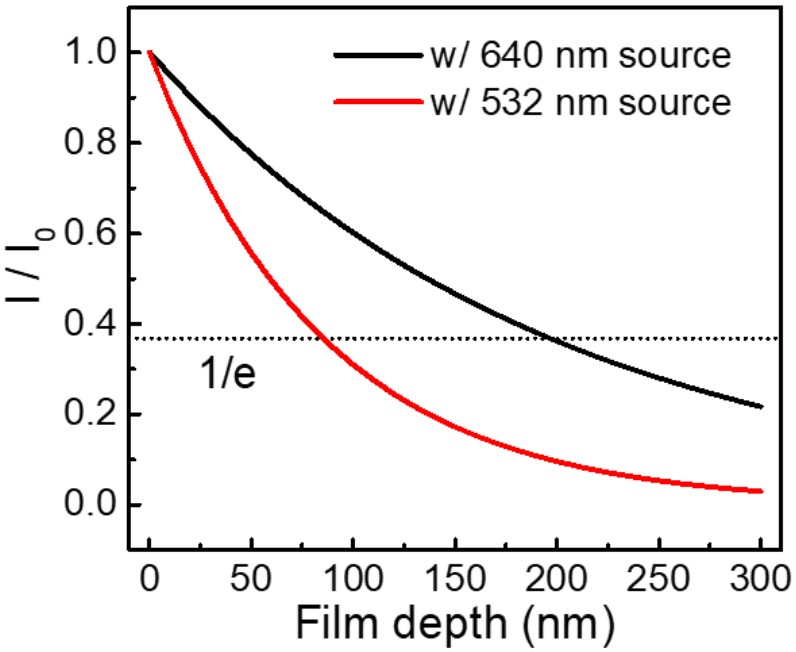

Figure S14 | Excitation wavelength dependant penetration depth. Decay of the beam intensity according to Beer-Lambert's law with perovskite film depth with different excitation sources. The penetration depth is defined at the depth where the intensity decays to (1/e) of its initial value (horizontal dashed line)

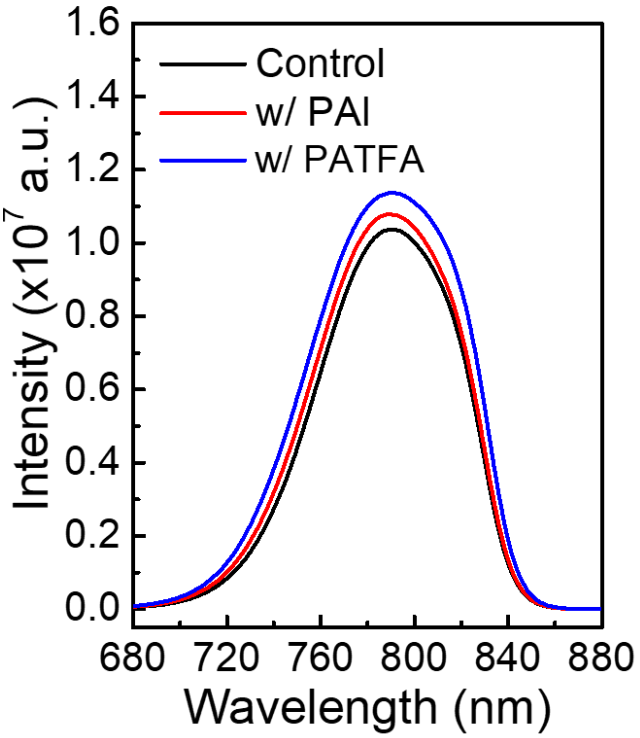

Figure S15 | Steady-state photoluminescence (PL) spectra of the perovskite films. PL spectra of the control and treated perovskite films on glass probed with an excitation wavelength of 640 nm.

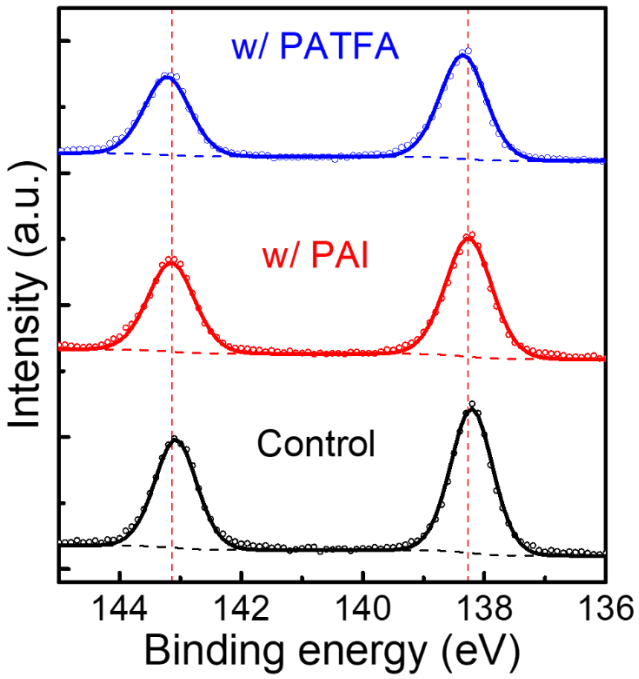

Figure S16 | X-ray photoelectron spectroscopy (XPS) measurements on the perovskite films. High resolution XPS spectra of the Pb 4f 5/2 and Pb 4f 7/2 peaks of the control and treated perovskite films. Red vertical dashed lines demarcate the peak positions of the PAI treated film.

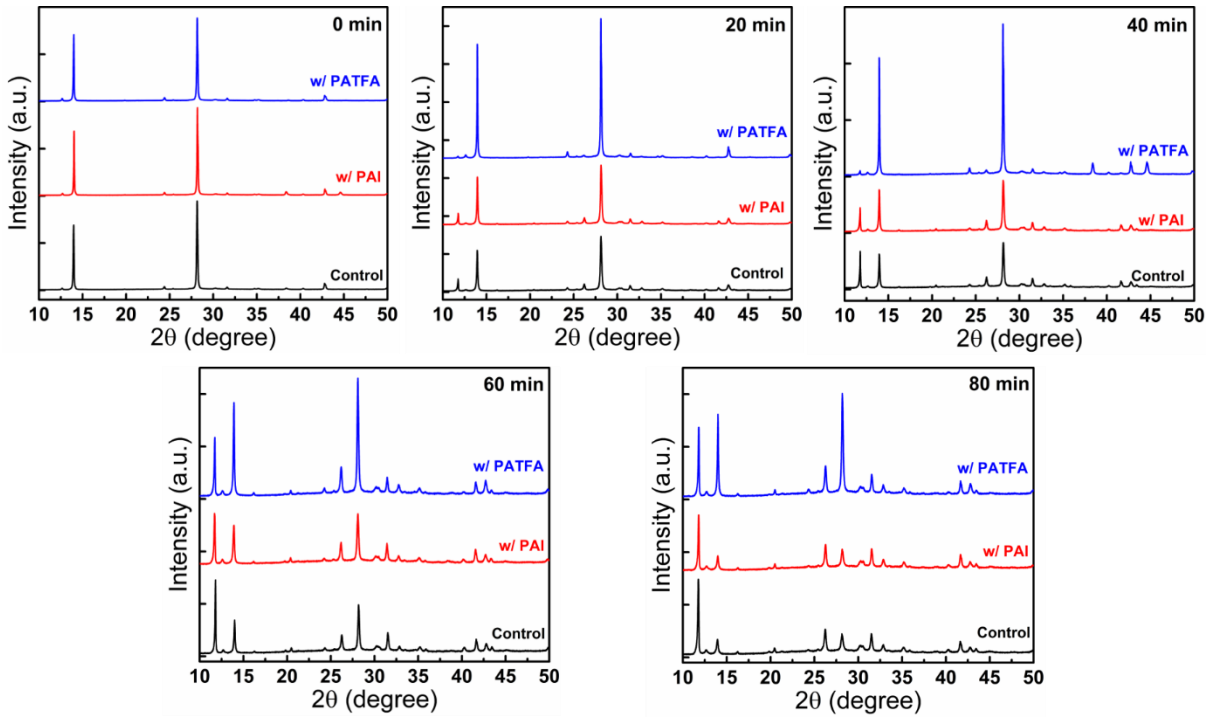

Figure S17 | X-ray diffraction (XRD) measurements on the perovskite films. XRD diffractograms of the control and treated perovskite films after different exposure times to iodine vapour.

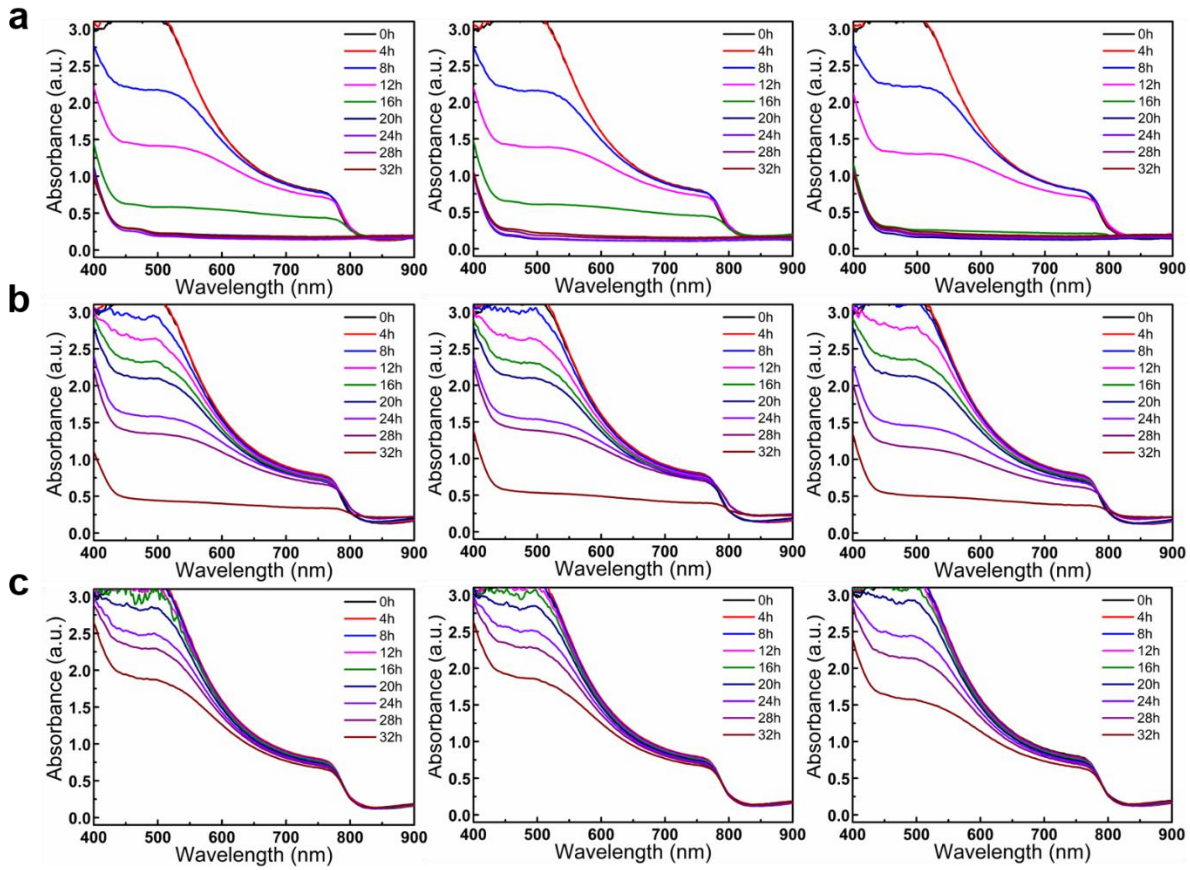

Figure S18 | Ultraviolet-visible spectroscopy measurements on the perovskite films. a, control, **b**, w/ PAI and **c**, w/ PATFA treatment**.** Absorption spectra of the control and treated perovskite films after different exposure times to RH 75 ± 10 %.

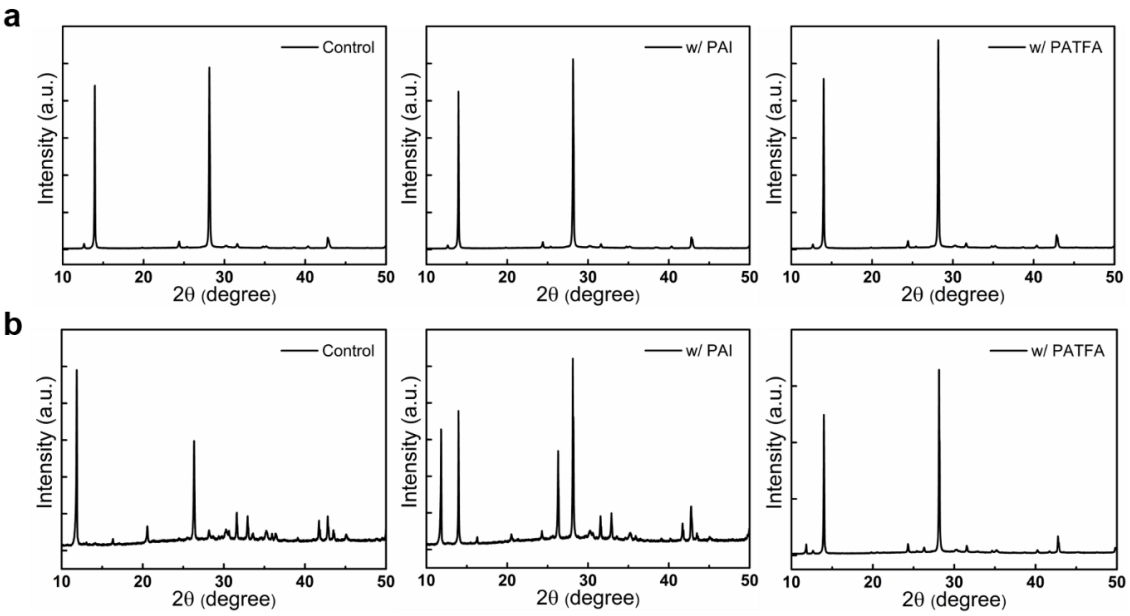

Figure S19 | X-ray diffraction (XRD) measurements on the perovskite films. X-ray diffractograms of the control and treated perovskite films **a,** before and **b,** after exposure to RH 75 ± 10 % for 32 h.

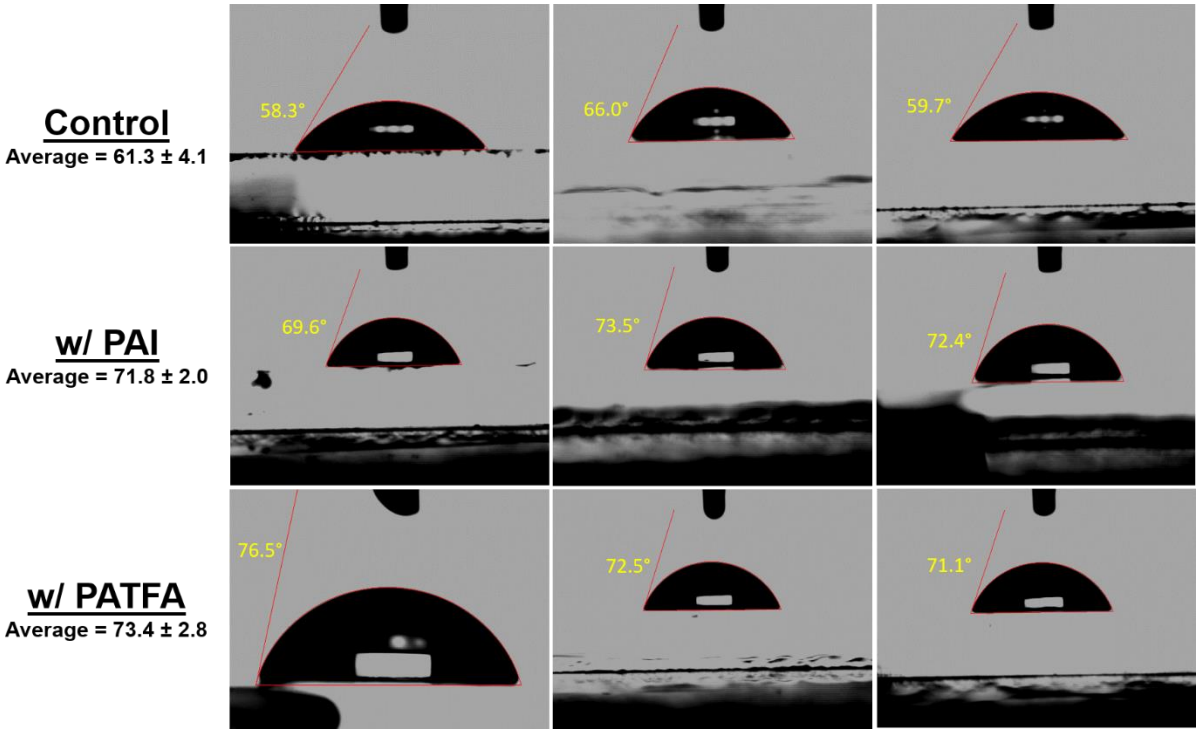

Figure S20 | Contact angle measurements of the perovskite films. Water contact angles of the control and treated perovskite films. The averages for three films of each condition are included.

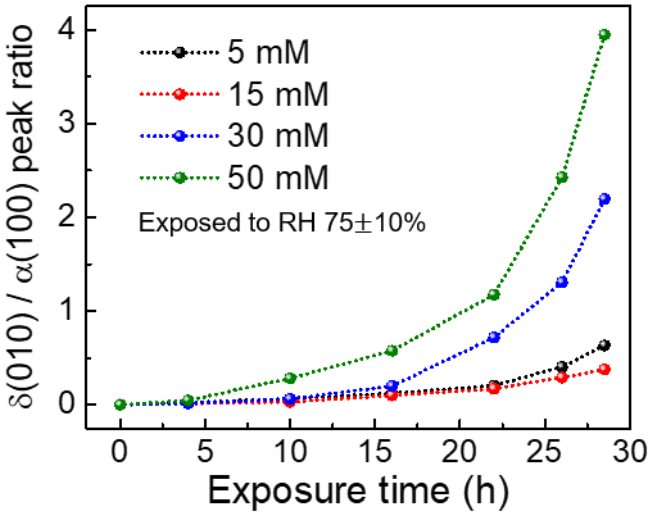

Figure S21 | α-phase stability of films with different PAI concentration. Hexagonal δ(010)-to-cubic α(100) x-ray diffraction (XRD) peak intensity ratio of the perovskite films as a function of exposure time to RH 75 ± 10 %.

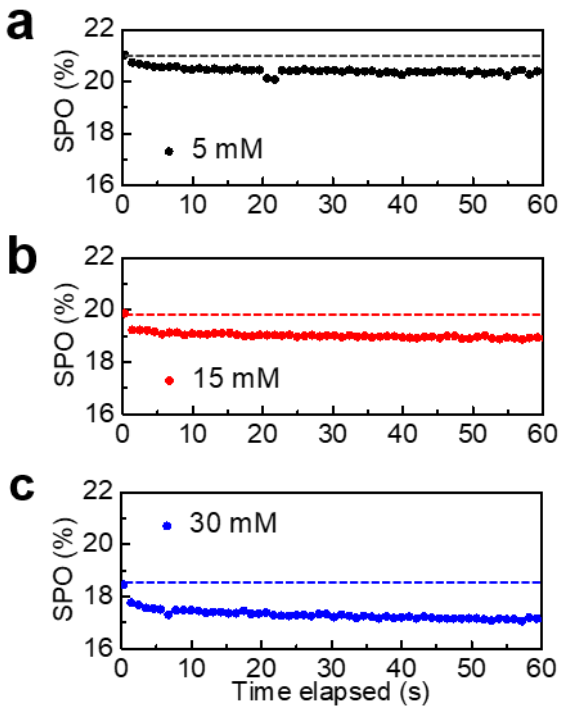

Figure S22 | Stabilized power output (SPO) of devices with different PAI concentration. SPO of devices treated with **a**, 5 mM, **b**, 15 mM, and **c**, 30 mM of PAI. Horizontal dashed lines mark the initial SPO.

Supplemental Tables

Table S1 | Surface treatment with organic iodide based salts. Summary of organic iodide based salts and their deposition conditions used to surface treat perovskite solar cells.

	Concentration (relative to I^-)	Deposition condition	Further processing	Reference
Octylammonium iodide	15 mM in IPA	5000 rpm	100°C anneal for 5 min	3
Dodecylammonium iodide	15 mM in IPA	5000 rpm	100°C anneal for 5 min	3
Phenethylammonium iodide	15 mM in IPA	5000 rpm	Dried in a vacuum oven for 24 h	3
Imidazolium iodide	35.7 mM in IPA	6000 rpm	70°C for 10 – 15 min	4
Ethylammonium iodide	17.3 mM in IPA	6000 rpm	70°C for 10 – 15 min	4
Guanidinium iodide	26.7 mM in IPA	6000 rpm	70°C for 10 – 15 min	4
Phenylalanine iodide	6 mM in IPA	4000 rpm	100°C anneal for 10 min	5
Octylammonium iodide	11.7 mM in IPA	5000 rpm	100°C anneal for 5 min	6
Butylammonium iodide	11.7 mM in IPA	5000 rpm	100°C anneal for 5 min	6
Phenethylammonium iodide	20 mM in IPA	5000 rpm	None	2

Table S2 | Photovoltaic parameters of control and treated devices. Average photovoltaic parameters of the control devices and devices treated with different ammonium cations.

	V_{OC} (V)	J_{SC} (mA cm^{-2})	FF	PCE (%)	Best PCE (%)
Control	1.077 ± 0.004	24.53 ± 0.08	0.771 ± 0.011	20.36 ± 0.36	20.95
PEAI	1.103 ± 0.004	24.51 ± 0.07	0.781 ± 0.002	21.10 ± 0.11	21.28
PEATFA	1.116 ± 0.004	24.49 ± 0.12	0.783 ± 0.003	21.41 ± 0.18	21.57
PAI	1.111 ± 0.006	24.45 ± 0.09	0.792 ± 0.012	21.50 ± 0.32	21.86
PATFA	1.124 ± 0.006	24.52 ± 0.08	0.796 ± 0.016	21.94 ± 0.45	22.72
OAI	1.106 ± 0.004	24.54 ± 0.14	0.772 ± 0.006	20.95 ± 0.23	21.42
OATFA	1.129 ± 0.005	24.47 ± 0.13	0.779 ± 0.009	21.51 ± 0.30	21.86

Table S3 | Distribution of the device photovoltaic parameters measured in reverse scan for different concentrations of PAI. Abbreviations are open-circuit voltage (V_{OC}), short-circuit current density (J_{SC}), fill factor (FF), power conversion efficiency (PCE), and stabilized power output (SPO).

	V_{OC} (V)	J_{SC} (mA cm^{-2})	FF	PCE (%)
5 mM	1.104 ± 0.005	24.53 ± 0.11	0.783 ± 0.009	21.19 ± 0.26
15 mM	1.099 ± 0.006	24.42 ± 0.18	0.743 ± 0.010	19.93 ± 0.38
30 mM	1.095 ± 0.008	23.70 ± 0.19	0.691 ± 0.012	17.92 ± 0.39

Supplemental References

1. Yang, W.S., Park, B.-W., Park, B.-W., Jung, E.H., Jeon, N.J., Kim, Y.C., Lee, D.U., Shin, S.S., Seo, J., Kim, E.K., et al. (2017). Iodide management in formamidinium-lead-halide – based perovskite layers for efficient solar cells. Science 356, 1376–1379.
2. Jiang, Q., Zhao, Y., Zhang, X., Yang, X., Chen, Y., Chu, Z., Ye, Q., Li, X., Yin, Z., and You, J. (2019). Surface passivation of perovskite film for efficient solar cells. Nat. Photonics 13, 460–466.
3. Min, H., Kim, M., Lee, S.-U., Kim, H., Kim, G., Choi, K., Lee, J.H., and Seok, S. Il (2019). Efficient, stable solar cells by using inherent bandgap of a-phase formamidinium lead iodide. Science 366, 749–753.
4. Alharbi, E.A., Alyamani, A.Y., Kubicki, D.J., Uhl, A.R., Walder, B.J., Alanazi, A.Q., Luo, J., Burgos-Caminal, A., Albadri, A., Albrithen, H., et al. (2019). Atomic-level passivation mechanism of ammonium salts enabling highly efficient perovskite solar cells. Nat. Commun. 10, 1–9.
5. Yang, S., Dai, J., Yu, Z., Shao, Y., Zhou, Y., Xiao, X., Zeng, X.C., and Huang, J. (2019). Tailoring Passivation Molecular Structures for Extremely Small Open-Circuit Voltage Loss in Perovskite Solar Cells. J. Am. Chem. Soc. 141, 5781–5787.
6. Kim, H., Lee, S.-U., Lee, D.Y., Paik, M.J., Na, H., Lee, J., and Seok, S. Il (2019). Optimal Interfacial Engineering with Different Length of Alkylammonium Halide for Efficient and Stable Perovskite Solar Cells. Adv. Energy Mater. 9, 1–8.